Research Article

Walied A. A. Mohamed*, Hala H. Abd El-Gawad, Hanan A. Mousa, Hala T. Handal, Hoda R. Galal, Ibrahem A. Ibrahem, Ahmed Atef El-Beih, Mona M. Fawzy, Mahmoud A. M. Ahmed, Saleh D. Mekkey, and Ammar A. Labib

Confinement size effect on dielectric properties, antimicrobial activity, and recycling of TiO_2 quantum dots *via* photodegradation processes of Congo red dye and real industrial textile wastewater

https://doi.org/10.1515/ntrev-2024-0001
received December 27, 2023; accepted February 29, 2024

Abstract: This article reports on the synthesis, characterization, and application of titanium dioxide quantum dots (TDS) for wastewater treatment. Three TDS samples were synthesized *via* a low-temperature precipitation method with calcination at 280°C (TDS1), 290°C (TDS2), and 300°C (TDS3). Characterization techniques such as X-ray powder diffraction, X-ray photoelectron spectroscopy, and transmission electron microscopy confirmed the high crystallinity, purity, and quantum confinement of the TDS with sizes of 3.1, 5.5, and 8.5 nm, respectively. The photocatalytic activity of TDS was evaluated by degrading Congo red dye under xenon lamp irradiation. TDS1, with the smallest size of 3.1 nm and the largest bandgap of 3.09 eV, showed the highest photodegradation rate of 22.49×10^{-3} S^{-1}. TDS1 also showed effective degradation of real industrial textile wastewater under sunlight over nine repeated cycles of use. The antibacterial activity of TDS against *Bacillus subtilis* and *Candida albicans* was demonstrated, with the highest inhibition by TDS1 attributed to its higher surface area. Overall, the study shows the high photocatalytic and antimicrobial potential of synthesized TDS, especially the smallest 3.1 nm TDS1 sample. The recycling results also showcase the reusability of TDS for wastewater treatment.

Keywords: quantum dots size, low-temperature modified precipitation method, industrial textile wastewater

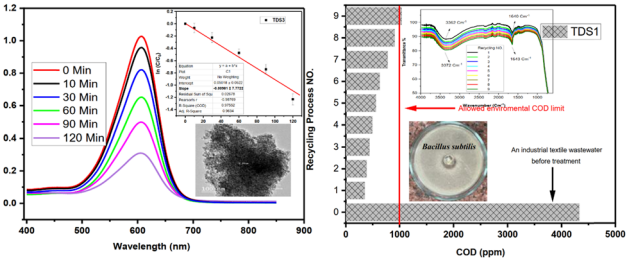

Graphical abstract

*** Corresponding author: Walied A. A. Mohamed**, Photochemistry and Nanomaterials Lab, Inorganic Chemistry Department, National Research Center, Cairo, 12622, Egypt, e-mail: waliedfx@yahoo.com, tel: +201005273874
Hala H. Abd El-Gawad: Department of Chemistry, Faculty of Science and Arts, King Khalid University, Mohail, Assir, Saudi Arabia, e-mail: habduljwaad@kku.edu.sa
Hanan A. Mousa: Photochemistry and Nanomaterials Lab, Inorganic Chemistry Department, National Research Center, Cairo, 12622, Egypt, e-mail: hmousa3@hotmail.co.uk
Hala T. Handal: Photochemistry and Nanomaterials Lab, Inorganic Chemistry Department, National Research Center, Cairo, 12622, Egypt, e-mail: hally.handal@gmail.com
Hoda R. Galal: Photochemistry and Nanomaterials Lab, Inorganic Chemistry Department, National Research Center, Cairo, 12622, Egypt, e-mail: hrgalal@hotmail.com
Ibrahem A. Ibrahem: Chemistry Department, Faculty of Science, Al-Baha University, Al-Baha 1988, Saudi Arabia, e-mail: Iali@bu.edu.sa
Ahmed Atef El-Beih: Department of Chemistry of Natural & Microbial Products, National Research Centre, Cairo, Egypt, e-mail: aae2eg@yahoo.com
Mona M. Fawzy: Egyptian Drug Authority (EDA)-Mansouria, Giza, Egypt, e-mail: monafawzy_sc@yahoo.com
Mahmoud A. M. Ahmed: The Public Authority for Applied Education and Training, Ardiya Safat, Kuwait, e-mail: mahmoud202000@yahoo.com
Saleh D. Mekkey: Department of Chemistry, College of Sciences and Arts, Northern Border University, Rafha, 91911, Saudi Arabia, e-mail: Saleh.Mekkey@nbu.edu.sa
Ammar A. Labib: Photochemistry and Nanomaterials Lab, Inorganic Chemistry Department, National Research Center, Cairo, 12622, Egypt, e-mail: ammar_al@yahoo.com

1 Introduction

Water is essential for life, but it is also vulnerable to pollution from various sources, such as industrial effluents, agricultural runoff, and urban waste. Among the pollutants that pose severe threats to human health and the environment are organic compounds, such as dyes, pharmaceuticals, pesticides, and other chemicals, that are resistant to conventional treatment methods. Therefore, there is a need for alternative and effective technologies to remove these contaminants from wastewater and restore water quality [1–5]. One of the promising technologies is photocatalysis, which uses light and a semiconductor catalyst to initiate oxidation and reduction reactions that can degrade organic pollutants into harmless products, such as water, carbon dioxide, or other simple molecules. Photocatalysis has several advantages, such as low cost, environmental friendliness, high efficiency, and applicability under mild conditions. However, there are also some challenges, such as the limited light absorption, the high recombination rate of photogenerated charge carriers, and the low stability and recyclability of the catalysts [6–9]. In recent years, significant progress has been made in the field of photocatalysis for wastewater treatment, with the development of novel catalysts, reactor designs, and process optimization. This article aims to review the recent research on photocatalysis for wastewater treatment, focusing on the following aspects: (1) the types and sources of organic pollutants in wastewater; (2) the principles and mechanisms of photocatalysis; (3) the synthesis and characterization of various photocatalysts, including metal oxides, metal sulfides, carbon-based materials, and hybrid composites; (4) the factors affecting the photocatalytic performance, such as light source, pH, temperature, catalyst dosage, and coexisting substances; (5) the design and operation of different photocatalytic reactors, such as batch, continuous, and hybrid systems; and (6) the evaluation and comparison of the photocatalytic efficiency, stability, and cost-effectiveness. The article also discusses the challenges and opportunities for the future development of photocatalysis for wastewater treatment [10–17].

The classification of dyes can be done in two different ways: based on their chemical structure or based on their method of application. Chemically, dyes can be either organic or inorganic compounds, and each category can have natural or synthetic variants. Application-wise, dyes can be anionic, direct, or dispersed, depending on the type of fiber they are used to color, such as protein, cellulose, or polyamide. However, these two classifications are not mutually exclusive, as some dyes belong to more than one coloristic group or can be applied to multiple substrates, while others are specific to a single group or substrate. The Color Index uses both classifications to catalog all the dyes and pigments that are commercially available for various coloration applications, such as textiles, plastics, paints, inks, and liquids [10–13,18–20].

Based on the photocatalytic process of organic pollutant degradation, the use of heterogeneous nano-photocatalysts made from metal oxides as raw materials is seen as a successful industrial wastewater treatment trend [21–24]. According to the functional claims made for metal oxide semiconductors, this technique has a wide bandgap, is environmentally friendly, is inexpensive, and is biocompatible. Furthermore, these compounds can break down a wide variety of pollutants when exposed to ultra violet (UV) light [25–27].

Titanium dioxide nanoparticles are often regarded as the most effective room-temperature photocatalyst among heterogeneous nanocatalysts due to their large band gap (3.20 eV) for the anatase phase. They are employed in the photodegradation of organic dyes, in addition to their usage in the treatment of industrial effluent and water [27–32].

Ten-nanometer-diameter titanium dioxide quantum dots (TDS) have unique physicochemical and luminous features that are not seen in macromolecules [33–35]. Because the influence of the quantum size is so crucial to photo and electrical parameters such as excitation energy and radiation lifetime, TDS preparation is of significant interest [36–38]. According to the boxed particle theory of quantization, shifts in particle size translate into shifts in electronic structure, with holes and electrons experiencing spatial constraints at the same time that energy levels are constrained. As the particle size of the produced quantum dot oxides decreases, the frequency at which they emit and absorb light changes dramatically [39–45]. In addition to their use as cell biomarkers [46,47], antibacterial drugs [48–51], antifungal agents [52,53], and in gene therapy [54,55], a promising new approach to treating cancer, TDS, has many other potential applications. Recent studies have shown that TDS may be employed in a wide variety of cutting-edge technologies, such as optoelectronics instruments, UV laser detectors, photodetectors, high-performance solar cells (about 60%), film transistors, and photodetectors [43,56–62].

In the present study, we investigated the structure, surface characteristics, and optical properties of thermally decomposed titania nanocrystallites (TDS) subsequent to their formation. Further advances in the tunable absorption assessment and quantification of the photocatalytic activity were accomplished *via* systematic measurement and quantification of the optical deterioration of dyes under varied illumination conditions. Additionally, the

antimicrobial properties of all synthesized samples were examined *in vitro* against the gram-positive bacterium *B. subtilis*, the gram-negative bacterium *Escherichia coli*, and the yeast *Candida albicans*.

Furthermore, we devised a straightforward and cost-effective methodology for synthesizing TDS in the anatase crystalline form. Various TDS samples were fabricated utilizing thermal techniques, the intricacies of which have been elucidated herein. Several variants of the Congo red dye could be produced by harnessing quantum dots in conjunction with irradiation from a xenon photoreactor in a photocatalytic process. Our investigation has also reliably estimated the recyclable characteristics of the TDS samples employed in the photocatalytic mineralization of industrial textile effluent under solar illumination conditions. In summary, our systematic analyses have provided novel insights into the structure–property relationships of thermally synthesized TDS photocatalysts and their potential applications in wastewater remediation.

2 Experimental

2.1 Materials

All the compounds that were used in this study were of analytical grade and had not undergone any purification processes. All chemicals were supplied by Fisher and Sigma Company. Isopropyl alcohol, with a purity level of 99.5%, was supplied by Fisher Company. Titanium(IV) isopropoxide (TTIP) had been supplied by Fluka Company. In the dye companies, Congo red dye had been produced from the manufacturing site at one of the textile processing and dyeing factories at Al-Obour industrial city, Cairo, Egypt, as a local market dye. The cetyl trimethyl ammonium bromide (CTAB) industrial powder was supplied by Fluka Company. In addition, deionized water was utilized.

2.2 Method of preparation

TDS samples by low-temperature precipitation method rather than any other method because at low temperature the observed size is the minimum size can be obtained while at high temperature the phase observed of TDS sample observed have larger size than that obtained at low-temperature. Also, most common methods, such as sol–gel and hydrothermal methods, produced nano-TiO_2 with a larger size than that obtained by the low-temperature precipitation method. Low-temperature TDS samples precipitated using a novel method. Using a syringe, 6.0 mL of TTIP was dispensed into a 250 mL beaker containing 180 mL of isopropyl alcohol, and the mixture was stirred continually at 0°C for over 60 min to create solution A (pH = 7). After 24 h at room temperature (25°C), a white powder is produced by slowly adding 0.03 mol of CTAB to solution (A). The dry white powder was taken out of the crucible and placed in the mortar. The samples were coarsely crushed, then deposited in an aluminum oxide crucible. Subsequently, the samples were subjected to the calcination process in a muffle furnace for 45 min at 280, 290, and 300°C, generating TDS1, TDS2, and TDS3, respectively.

2.3 Characterization

The crystalline characteristics of the produced materials were evaluated using the Cu-Kα criteria by PANalytical X'pert professional MPD (Netherlands), where Cu-Kα radiation = 0.154 nm, 40 m, A50 kV; data were recorded in 0.017 s per step by using Philips, X' pert MPD, Netherlands. X-ray photoelectron spectroscopy (XPS) was measured at ultra-high vacuum (UHV) on K-ALPHA from Thermo Fisher Scientific (USA) with X-ray (monochromatic) where spot size is 400 µm at pressure 10^{-9} mbar and Al K-alpha radiation −10 to 1,350 eV at narrow spectrum 50 eV with spectrum pass energy reached 200 eV, and the quantum dot samples' form and particle size were studied using high-resolution transmission electron microscopy (HRTEM) (Philips/FEI BioTwin CM120, USA). Shimadzu, UV 2600i (Japan), a parameter measurement system, was used to measure the UV–Vis absorption spectrum. The precise surface area of the ready catalysts was determined using the Brunauer–Emmett–Teller (BET) technique from the surface homogenization curve of N at 78 K using a microTris-tar 3000 (USA) from Micromeritics Instrument Corporation.

When the TQD samples are ready at 160°C for 1 h, by employing the following equation: $S = 6/\mathrm{dx}\rho$, the specific surface area is calculated: where d is the mean particle diameter, ρ is the three TiO_2 density values estimated (4.30, 3.89, and 3.43 g/cm^3) for TDS1, TDS2, and TDS3 samples, respectively, and S is the BET-surface area specific.

A xenon photoreactor with a water-cooling system is used for the photodegradation operations to avoid the lamp's temperature going too high. The wavelength of the xenon light lamp ranges from 200 to 1,100 nm with moderate power at 100 W/cm^2 in the presence of TDS samples, Congo red dye, and industrial textile effluent, measured using a multiparameter benchtop photometer.

The COD was measured with the COD C99 Series Multiparameter Desktop Photometer, Hanna, USA. Photocatalytic

activity was evaluated by total organic carbon (TOC) from Analytik Jena (multi N/C3100), Germany. Recycled TDS used in the recycling processes was illustrated by means of Fourier transform infrared spectra (FTIR), which were recorded using a Jasco, FTIR-4600, USA, to detect any changes observed for the prepared catalyst after each recycling process.

2.4 Photocatalytic efficiency of TDS

The photocatalytic technique was used for assessing photocatalytic efficacy and enhancing photodegradation of Congo red dye as a model artificial dye using a xenon photoreactor (100 W) with a wavelength limit of 200–1,100 nm: 0.25 g of TDS were distributed in 500 mL of dye solution (5×10^{-5} M, pH = 6.8) [63–65]. Then TDS was added to the dye and stirred for 30 min in the dark to verify the adsorption/desorption equilibrium. The last step is to remove any leftover catalyst particles from the solution by immediately centrifuging using Thermo MEGAFUGE 16 for 30 min at 12,000 rpm.

2.5 Photocatalytic activity by sunlight

In order to assess how well photocatalysis works, industrial textile effluent from a dying plant with a pH in the region of 6.9 is treated immediately under direct sunlight. Throughout the research, the daily dosage of UV radiation was 4.7 mW/Cm^2, and the dose of visible light received during the middle of the day was 1,635 mW/Cm^2. Quantification of the photocatalytic activity of an unusually active sample was accomplished by examination of the amount of carbon dioxide present at time *t*.

2.6 Recycling processes

The recycling process of TDS as photocatalysts was validated and estimated nine times by utilizing spectrophotometry to measure the photodegradation rate of all the photodegradation processes evaluated for dyes using a xenon photoreactor and sunlight. This was done in order to determine how quickly the dyes broke down in the presence of light.

TOC and COD (chemical oxygen demand) investigations were also used as a method for assessing the maximum percentage across all the photocatalytic processes that were found.

2.7 *In vitro* antimicrobial activity

Antimicrobial activity of different TDS samples was evaluated against pathogenic Gram-negative bacterium (*Salmonella enterica* ATCC 25566), Gram-positive bacterium (*B. subtilis* ATCC6633), fungus (*Fusarium solani* NRC15), and fungal yeast (*C. albicans* ATCC 10231) by the agar spreading technique carefully.

Fungal yeast and bacteria were obtained from the American Type Culture Collection, while the isolated fungal was obtained from the culture collection from the Chemistry of Natural and Microbial Products Department, National Research Center, Egypt. At least two passes for the microorganisms were done to ensure viability and purity. The fungi were grown on a potato dextrose agar medium, while the bacteria were grown on a nutrient agar medium. The antimicrobial assay used the spreading technique [66]. In these experiments, microbial suspension of fungus or bacterium was suspended, swabbed in sterile distilled water, and adjusted to McFarland No. 0.5 as standard turbidity. Then, the microbial suspension was spread on a nutrient agar medium for bacteria or on potato dextrose agar medium for fungi.

The inoculated agar was poured into an assay plate with a 5 cm diameter, and it was then allowed to cool on a level surface. Once the solidification of the medium is observed, 4 mm diameter agar slices were made, and 10 mg of the TDS-prepared samples were placed into each one. The inoculated agar plates were incubated for a day at 37°C for bacteria and 3 days at 27°C for fungi. The antimicrobial effect was estimated and evaluated by measuring the diameter of the inhibition zone around samples in millimeters.

3 Results and discussion

3.1 X-ray powder diffraction (XRD)

Crystallographic characteristics of the produced quantum dot samples were studied by inverse XRD analysis, as shown in Figure 1. Complete indexing of XRD data was performed on the TDS structure (JCPDS-ICDD file 84-1285). The (101), (112), (200), (105), and (213) planes correspond to the optical phenomena peaks seen at 2θ of 25.3°, 37.8°, 48.0°, 55.0°, and 62.6°, respectively. The high purity of the TDS samples' crystalline nature in the anatase phase under the testing conditions was shown by the absence of distinct impurity characteristic peaks in different second stages.

Figure 1 also depicts the TDS-supported packing structure of Rietveld screens. The Scherrer equation was used to calculate an approximate crystallization size for the produced samples:

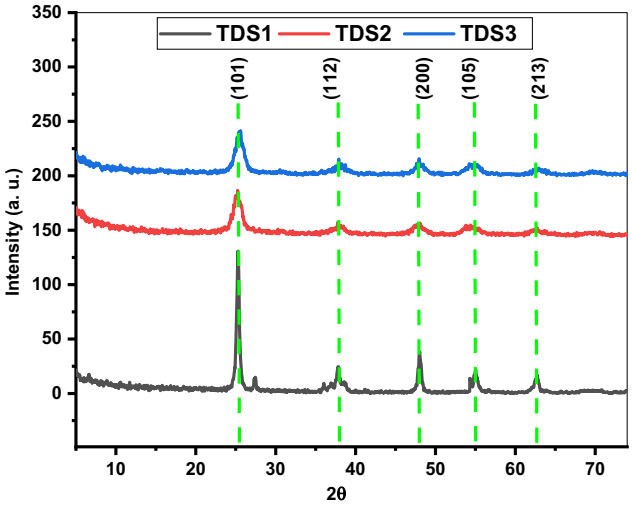

Figure 1: XRD pattern of different TDS samples.

Table 1: Lattice parameters (*a*, *c*), unit cell volume (*V*) data of TDS samples

Sample	*a* (Å)	*c* (Å)	*V* (Å^3)	Crystallite size (nm)
TDS1	3.7090	9.4090	134.8995	3.1
TDS2	3.7165	9.4400	134.9663	5.5
TDS3	3.7209	9.4860	135.2222	8.5

$$D = \frac{k\lambda}{\beta \cos\theta}, \tag{1}$$

where k is the wavelength of the radiation employed in Cu-Kα detectors (0.15406 nm), β is the half-maximum breadth of the peak, 2 h is the maximum angle of the optical phenomena, and K is Scherrer's constant (≈ 0.9).

Figure 1 depicts the situation. Common crystallization sizes were 3.1, 5.5, and 8.5 nm for samples TDS1, TDS2, and TDS3, respectively, indicating a minor increase in the estimated crystallization sizes when the temperature is increased, as shown by the obtained values.

Table 1 and Figure 2 show the results of the Rietveld refinement analysis performed on the XRD data using Full-Prof software, which yielded the lattice constant and unit cell volume. The Rietveld refinement profiles of all the TDS-prepared samples matched the experimental data exactly. The Ti^{4+} ion (sixfold coordination, VI) has an ionic radius of 0.601 in TDS1, 0.606 in TDS2, and 0.613 in TDS3. The close difference in the ionic radii and the competitive effect between them are responsible for the significant increase in the unit cell volume of TDS-prepared samples, which is caused by the decreasing crystal size of the TDS-prepared samples.

3.2 XPS

The TDS1 surface characterization was confirmed by XPS. Oxygen, carbon, and titanium were detected in the observed spectra. The binding energy (BE) of the C1s photoelectron peak was observed at 280 eV, which is stronger for TDS1 (Figure 3(d)), while the XP spectrum of TiO_2 in the Ti 2p deconvoluted into four Ti 2p peaks, as shown in Figure 3(b); Ti^{3+} 2p3/2 at 448.88 eV, Ti^{3+} 2p1/2 at 459.80 eV, Ti^{4+} 2p3/2 at 460.92 eV, and Ti^{4+} 2p1/2 at 465.08 eV EB irradiation.

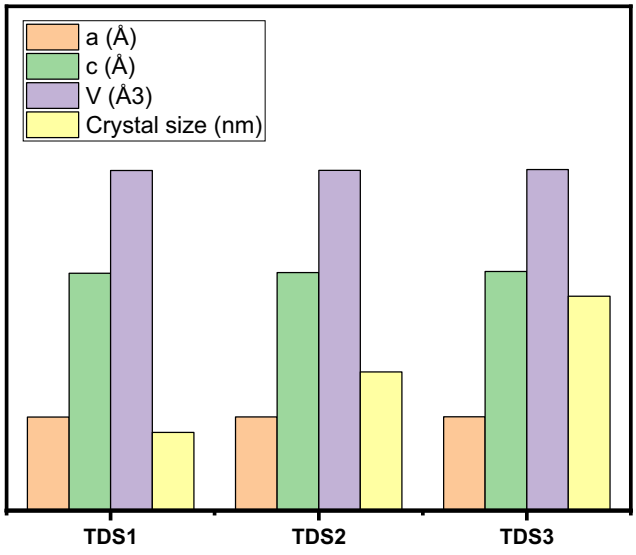

Figure 2: Variation of lattice parameters (*a*) and (*c*) and unit cell volume (*V*) of different TDS samples.

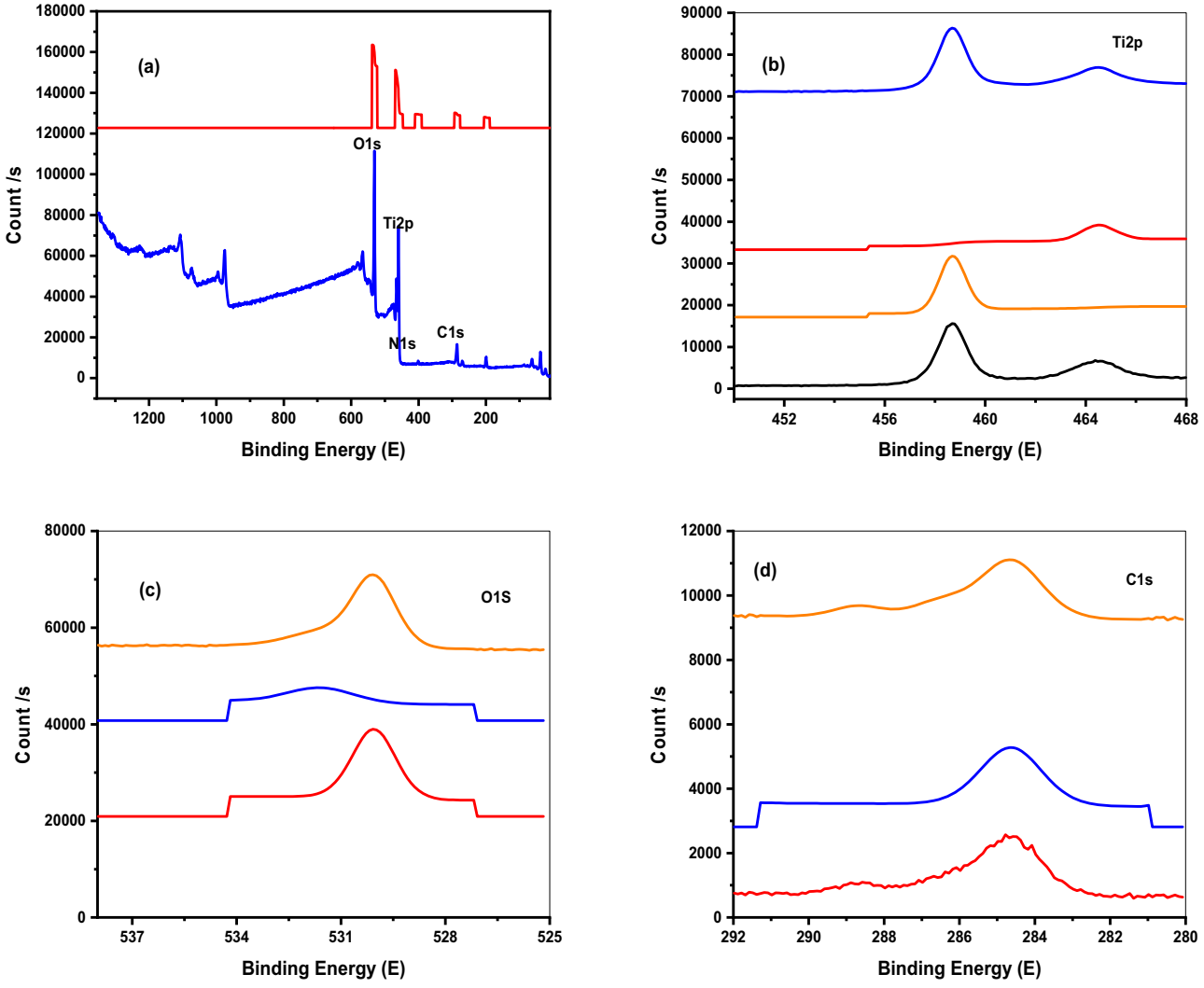

Figure 3: XPS of (a) TDS1, (b) Ti2p, (c) O1s, and (d) C1S.

Particularly, the concentrations of Ti^{4+} decreased with EB irradiation, whereas the concentrations of Ti^{3+} increased. The Ti^{3+} amount on the surface of TDS1 plays an interesting role due to TDS1 doping with polymer atoms. In Ti^{3+}, trapping of the photogenerated electrons was observed, thereby inhibiting the majority and minority carrier's recombination [67,68]. Also, the binding states of oxygen in TDS1 were determined where the O1s XPS peak was observed to three peaks as shown in Figure 3(c) at 529.90, 529.50, and 528.15 eV. The TDS1 survey spectra contain the O 1s and Ti 2p peaks of the titanium dioxide, C1S, and N1S (Figure 3(a)).

3.3 Transmission electron microscopy (TEM)

The shape and length of the TDS particles in the arranged samples were investigated by HRTEM, a technique that allows for direct imaging of the atomic structure of samples. Figure 4 shows the HRTEM images of the samples, which confirm the formation of ultrafine nanoparticles. The nanoparticles exhibit high crystallinity and anisotropic morphology, with ellipsoidal and elongated shapes. The average diameters of the nanoparticles in the samples TDS1, TDS2, and TDS3 are 3.1, 5.5, and 8.5 nm, respectively.

The annealing temperature of 70°C was reached, and the particle length of the generated samples increased slightly compared to the crystallite length. The particle length for TDS1, TDS2, and TDS3 was 3.1, 5.5, and 8.5 nm, respectively, at this temperature. The preparation method and the stabilizing solvent were effective in preventing nanoparticle coagulation and maintaining the particle size below 10 nm; the threshold for quantum confinement effects and some agglomeration was observed, which was attributed to the small size of the particles.

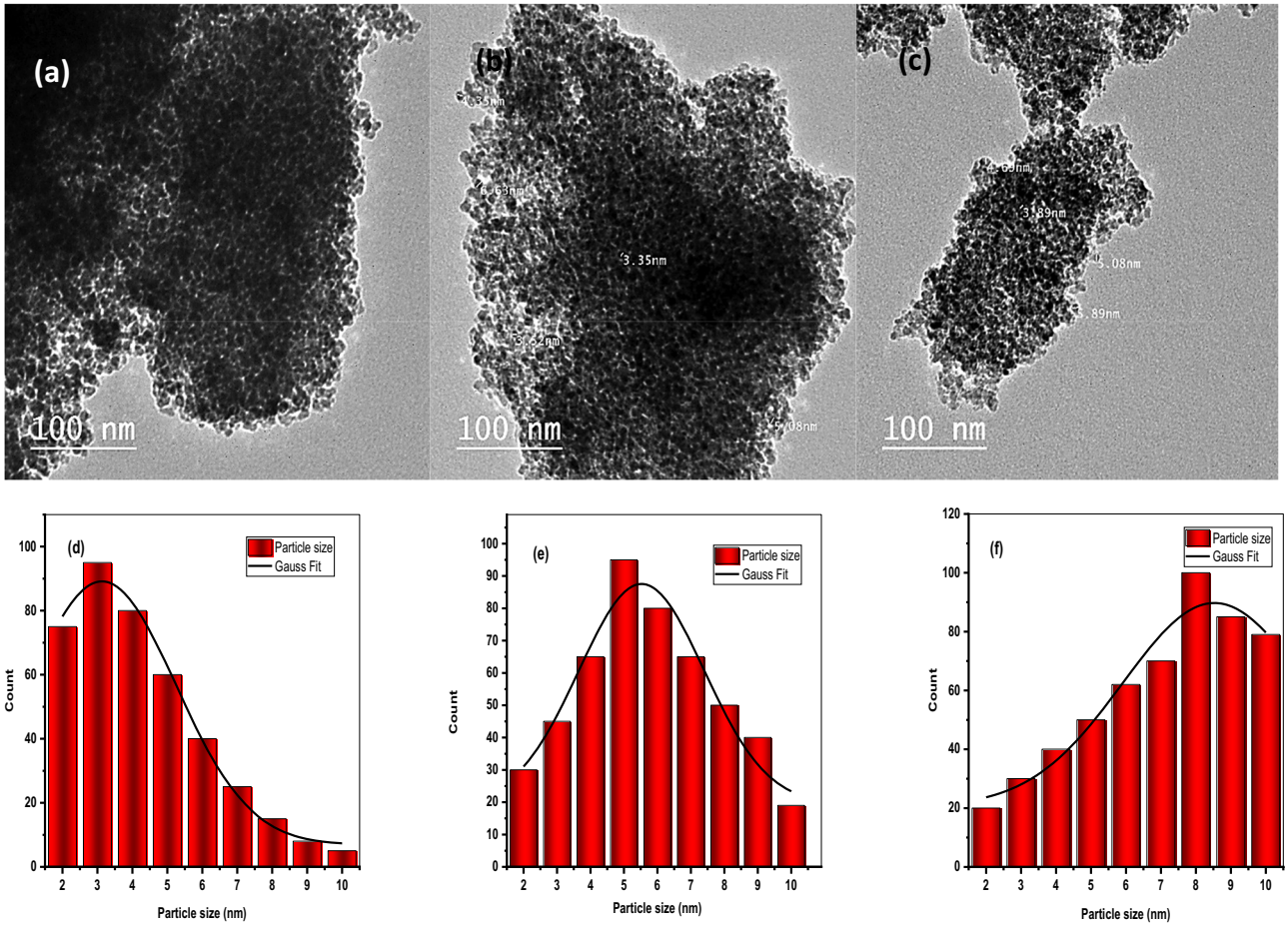

Figure 4: (a)–(c) TEM of TDS samples, and (d)–(f) particle size distribution map.

From previous results observed (XRD and HRTEM), in the case of quantum dots, the photocatalytic activity increases as the particle sizes decrease which observed from XRD and HRTEM which led to increases in the band gap, which led to an increase in the photocatalytic activity because there is an inverse relationship between particle size and the photocatalytic activity according to literature and our previous work [28,65,69,70].

3.4 SEM

The FE-SEM images of TDS samples are shown in Figure 5, where the particle size reached more than 30 nm after just 1 day. In order to keep the nanoparticles below the quantum dots limit of 10 nm, it was necessary to make use of powerful stabilizing solvents that prevent coagulation. These solvents played a crucial role in preserving the desired nanoscale size by providing a stable microenvironment, thereby aligning with the critical requirements for quantum dot applications [71,72].

3.5 FTIR analysis

The results of an investigation into the chemical composition of TDS samples are shown in Figure 6. Stretching vibrations have been seen in Ti–O–Ti; however, the cause of these vibrations has not been determined. These vibrations may be imagined as a wide band with a frequency range of 400–900 cm^{-1}. It has been determined that bending and stretching vibrations in the hydroxyl group are responsible for the bands that may be seen at 1636.008–1632.025 cm^{-1} and 3341.111–3361.225 cm^{-1}. It is possible to minimize the mass of the molecule by redistributing the height to the facets, which have greater wave numbers [73,74].

Relative banding system changes in the intensities of absorption bands and frequency shifts reflect changes in a

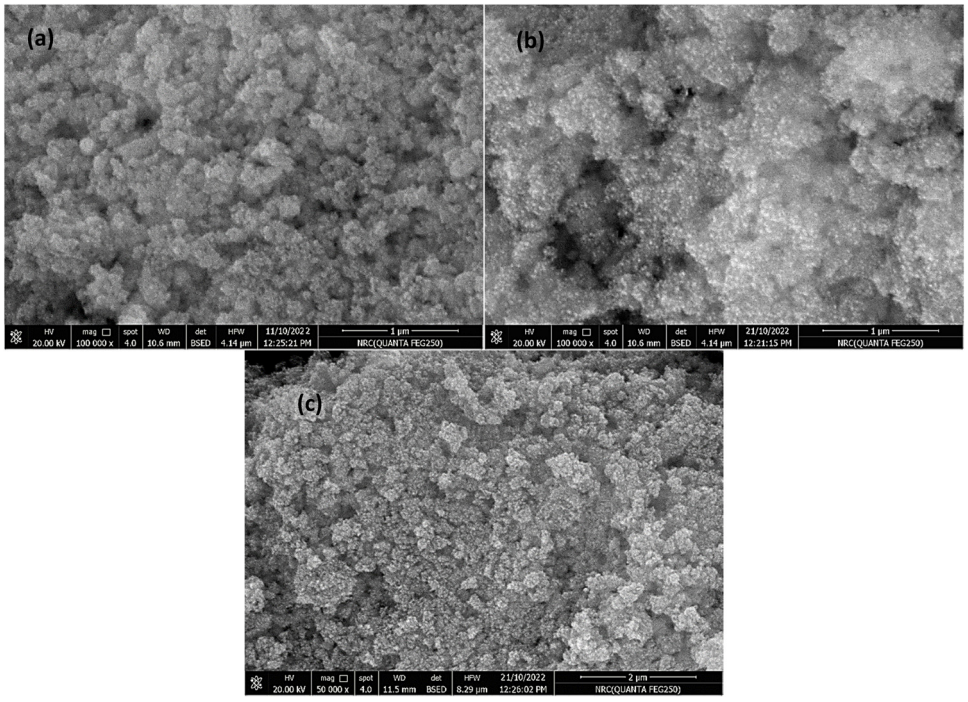

Figure 5: The FE-SEM images of (a) TDS1, (b) TDS2, and (c) TDS3.

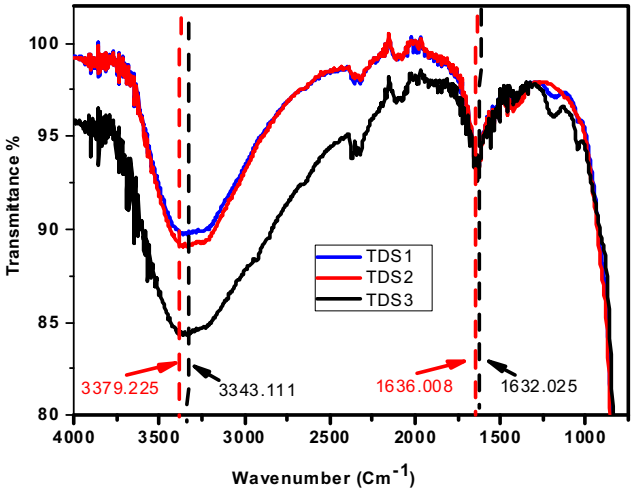

Figure 6: FTIR spectrum of different TDS-prepared samples.

pattern that is controlled by either the chemical form of the field or its surroundings [70,75]. It is possible that the wavenumbers and vibration frequency will increase if the molecule in question has a much lower mass.

3.6 Band gap

The determination of bandgap energies for the TDS samples was carried out utilizing the Kubelka–Munk (KM) function, an analytical technique well-established in the field of materials science. As illustrated in Figure 7, the KM analysis yielded bandgap energies of 3.09, 3.03, and 2.97 eV for TDS1, TDS2, and TDS3, respectively. These values provide insight into the electronic structure of the TDS materials and how their photocatalytic properties may vary with nanoparticle size.

In addition, the BET method was employed to ascertain the specific surface areas of the TDS samples, obtaining

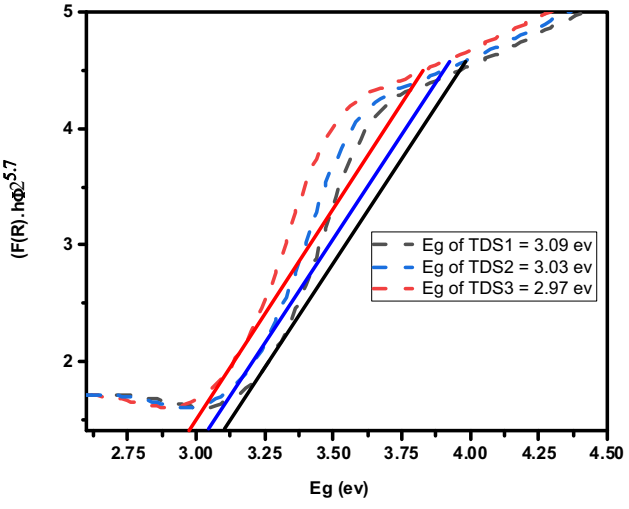

Figure 7: Tauc's plot, bandgaps, and diffuse reflectance of different TDS-prepared samples.

values of 357.14, 325.20, and 262.23 m^2/g for particle sizes of 3.1, 5.5, and 8.5 nm, respectively. The inverse relationship between surface area and particle size is ascribed to the greater relative surface exposed in smaller nanoparticles. Furthermore, the photocatalytic efficacy of TiO_2 materials is known to deteriorate rapidly due to high rates of recombination between photoexcited conduction band electrons and valence band holes. Strategies to mitigate this effect remain an active area of research, with controlled doping and nanostructuring approaches currently being investigated to prolong charge carrier lifetimes and thereby enhance photocatalytic performance.

3.7 Photocatalytic processes

The photodegradation of Congo red dye by a xenon photoreactor was investigated using different TDS samples. The absorption spectra of the dye solutions at different irradiation times are shown in Figure 8(a)–(c). The photodegradation rates were calculated from the changes in the absorbance of the dye at its maximum wavelength. Figure 8(d) shows the kinetic diagram of the photodegradation process, which exhibits a linear relationship between $\ln(C_0/C)$ and the irradiation time, where C_0 and C are the initial and final concentrations of the dye, respectively. This diagram applies to all photodegradation processes. Additionally, it has been shown before [64,65] that the production of hydroxyl radicals is an essential step in the process of Congo red dye photodegradation. Using TDS catalysts for photodegradation of Congo red dye is an example of a proposed technique. When just the catalyst is exposed to light, excited electrons (e^-) are displaced to a higher energy level. At the same time, excited ions (h^+) are generated at the lower energy level of the previous level.

The photodegradation of the Congo red dye depends on the generation of hydroxyl radicals, and superoxide was found to be the reactive species. It has been proposed that the production of Congo red dye may be accomplished by the interaction of (e^-) and (h^+) radicals with oxygen dioxide and water. After that, it focused on the active species of the Congo red dye molecule to finish the breakdown process [76–79].

TiO_2 was substituted for TDS in the equations that describe the general photocatalytic activity. This was done so that the equations could be understood more clearly. TiO_2 at the quantum dots limit is less than 10 nm. According to the hypothesized mechanism for the photodegradation of Congo red dye in the presence of TDS precursors, the irradiation process for the produced photocatalysts (TDS) would cause electrons to be transferred from the valence band region to the conduction band area. This will take place when electrons move from the valence band area to the conduction band area. The valence band serves as the point of departure, whereas the conduction band serves as the destination in its entirety. Then, only a higher energy level is reached by the excited negative electron (e^-), while a positive hole (h^+) forms at a lower energy level. Therefore, one may consider these activities to be by-products of the photocatalytic process.

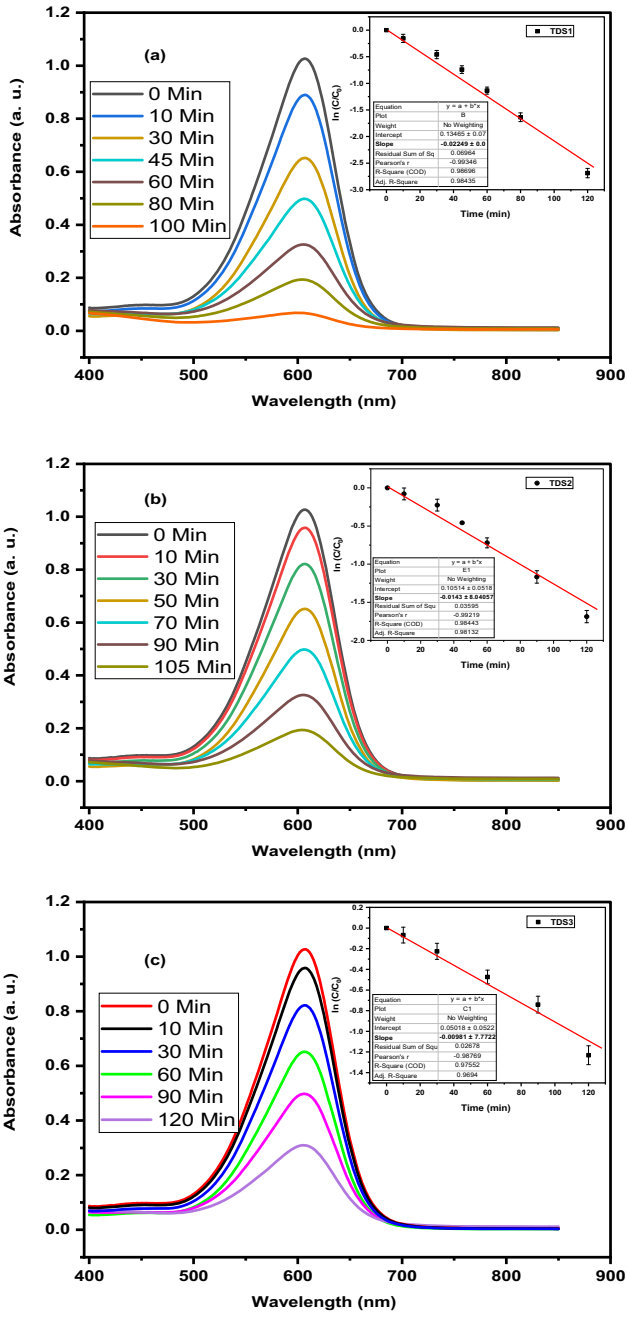

Figure 8: Absorption spectra and kinetics plot (a)–(c) of photodegradation process of Congo red dye.

Additionally, the general steps of the photocatalytic mechanism are examined, substituting TDS (identified as TiO_2 at the quantum dot threshold, less than 10 nm) by TiO_2 in the mechanism equations for improved clarity and comprehension in a scholarly discourse.

$$TDS + h\nu(UV) \rightarrow TDS(e^-)(CB) + TDS(h^+)(VB), \quad (2)$$

$$h^+ + H_2O \rightarrow {}^{\cdot}OH + H^+, \quad (3)$$

$$e^- + O_2 \rightarrow O_2^{\cdot-}, \quad (4)$$

$$H_2O + O_2^{\cdot-} \rightarrow HO_2^{\cdot} + {}^{\cdot}OH, \quad (5)$$

$$2HO_2^{\cdot} \rightarrow H_2O_2 + O_2, \quad (6)$$

$$H_2O_2 + O_2^{\cdot} \rightarrow {}^{\cdot}OH + OH^- + O_2, \quad (7)$$

$$\text{Dye} + {}^{\cdot}OH + O_2^{\cdot-} \rightarrow \text{Degraded organic dye}, \quad (8)$$

$$\text{Degraded organic dye} + {}^{\cdot}OH + O_2^{\cdot-} \rightarrow H_2O + CO_2. \quad (9)$$

In the proposed mechanism for the photodegradation of Congo red dye in the presence of TDS situated in the valence band region, the translocation of electrons from the valence band to the conduction band is induced by the irradiation process. Commencing in the valence band and culminating in the conduction band, this transference results in the electron ascending to a higher energy state within the excited negative electron (e^-) configuration. Simultaneously, a positive hole (h^+) emerges at a lower energy level. Consequently, these processes may be construed as consequential by-products of the photocatalysis process. Also, a schematic illustration of the photodegradation process is shown in Scheme 1.

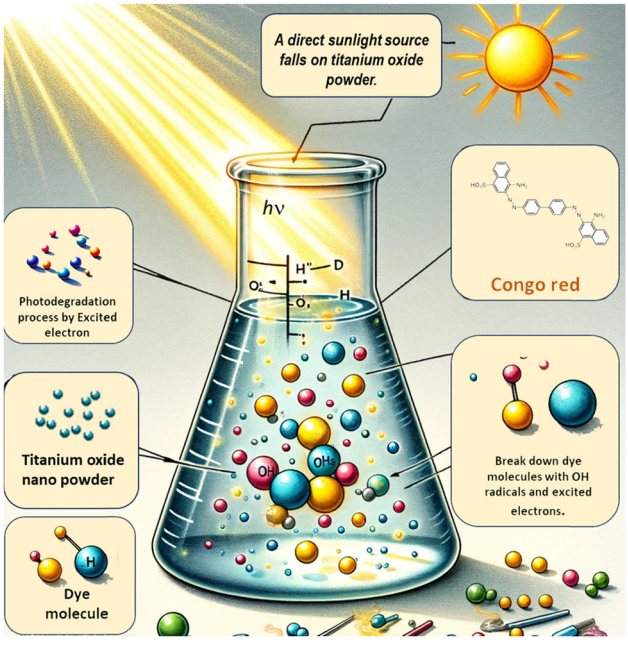

Scheme 1: A schematic illustration of the photodegradation process of Congo red dye in the presence of different TDS samples.

The rate of photodegradation of Congo red dye in a xenon photoreactor is about 2.5 times greater at TDS1 = $22.49 \times 10^{-3}\,S^{-1}$ than it is at TDS3 = $9.81 \times 10^{-3}\,S^{-1}$, and it is roughly 1.5 times quicker at TDS2 = $14.30 \times 10^{-3}\,S^{-1}$. According to the findings, photocatalytic performance rises with decreasing TDS size because this leads to an increase in surface area across all photodegradation processes. This is the conclusion drawn from the data. Even when contrasting the efficacy of various photodegradation processes, this observation is true. When the TDS size is decreased, the value of the band gap may be observed to rise to higher levels. These results give more indication that the quantum size impact of TDS photocatalysts has an influence on the photocatalytic activities that are taking place, as shown in Table 2.

3.8 Recycling processes

The photodegradation of a real industrial effluent with a high COD of 4,385 ppm was investigated using different cycles of recycling of the photocatalyst. The COD is a measure of the amount of oxygen required to oxidize the organic pollutants in water 1. The photocatalyst was a nanosized sample of TDS1 (3.1 nm), which was reused nine times. The recycling of the photocatalyst resulted in its accumulation and reduced its photodegradation efficiency. However, after nine cycles, the COD of the effluent was reduced to less than 1,000 ppm, which is the maximum permissible limit according to Egyptian Environmental Law 2. This indicates that the TDS1 sample was effective

Table 2: Photodegradation rate constant Kr, irradiation time of photodegradation of Congo red dye in the presence of different TDS samples with their crystallite sizes and Eg values

Sample	Kr S^{-1}	Irradiation time (min)	Crystallite size (nm)	Eg
TDS1	6.94×10^{-3}	100	3.1	3.09
TDS2	4.50×10^{-3}	105	5.5	3.03
TDS3	9.89×10^{-3}	120	8.5	2.97

in degrading the organic contaminants in the effluent [80,81]. The photodegradation rate of the TDS1 sample was determined by measuring the changes in its optical properties. The increase in the size of the TDS particles during the photodegradation process was attributed to the thermal effects induced by direct sunlight exposure. The sunlight not only provided the photons for the photodegradation reactions but also increased the temperature of the sample, which affected its morphology and stability.

Figure 9 shows that the total length of time spent in direct sunlight reached 9 h, and that as TDS increased in size as a result of accumulation, the rate at which it underwent photodegradation slowed down. Both of these findings are shown in the graph. The TOC investigation exhibited a similar behavior as the COD observation, as shown in Figure 10, with photodegradation rates of the real industrial effluent sample reducing to nine times recycling when the TDS1 sample was present. This result was consistent with the COD observation. Despite the fact that there was a photodegradation process by direct sunlight, these data show that the size of TDS particles rose during the recycling process and that this trend was reflected in the breakdown rate determined by the COD and TOC tests. This was the case despite the fact that the recycling process was carried out.

Figure 11 shows that the FTIR spectrum of the recyclability of the sample that was tested (TDS1) does not have an influence on the created catalyst until after nine cycles of recycling have been completed; nonetheless, these shifts are caused by agglomeration after recycling for several cycles. In the FTIR spectrum of TDS1, broad bands at 660 cm^{-1} indicate Ti–O–Ti bonds, while two bands at 1,640 and 3,362 cm^{-1} are related to the stretching and bending vibrations of O–H

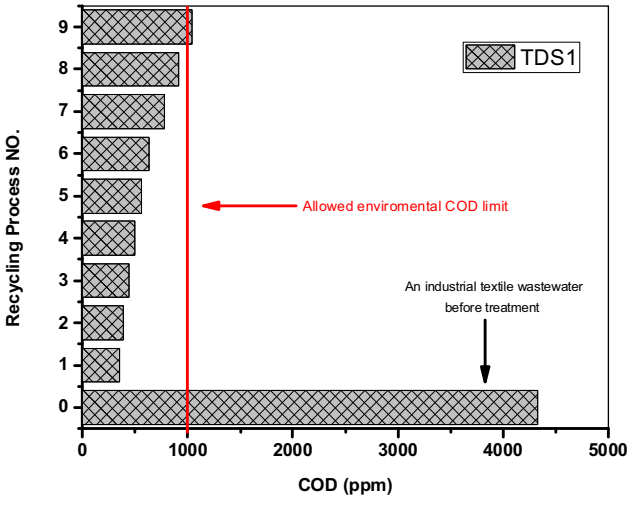

Figure 9: COD of solar irradiation for a real sample during the recycling process of the TDS1 sample.

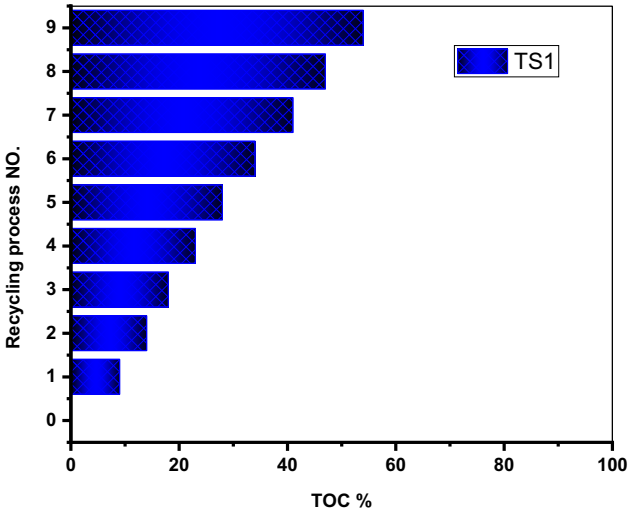

Figure 10: TOC of solar irradiation for a real sample during the recycling process of the TDS1 sample.

groups, respectively. After going through nine cycles of recycling, the O–H group band's stretching and bending vibrations shifted by 1,643 and 3,372 cm^{-1}, respectively.

From the above results, the performance of the TDS samples across multiple recycling cycles proven by both techniques FTIR and COD, where at COD analysis the real sample which have COD value at 4,385 ppm after each recycling process which including the same solar irradiation process for a 8 h, the COD value increases because the quantity of oxygen demand for COD analysis increases so the final COD value increases by increasing the number of recycling process till reached to the COD allowed limit according to the environmental law applied from the environment ministry (1,000 ppm). Just the COD value reached 1,000 ppm, the recycling processes stopped, and there is no need to continue because after that, it is not accepted environmentally and legally.

Also, TOC used to evaluate the performance of the TDS samples across multiple recycling cycles but depending on the decrease in the total organic content in the TDS samples across multiple recycling cycles till reached nearly less than 9% and after that we did not observe any variation in the decreasing value, so the recycling processes stopped and there is no need to continue because after that it is not accepted environmentally and legally.

The stability of the TDS samples across multiple recycling cycles provided by the FTIR spectrum, where there is no shift observed for the peaks of the TDS samples, which indicated that there is no phase change in TDS samples observed. The observed effect of the decrease in the intensity of FTIR refers to decreases in the active site on the prepared catalyst.

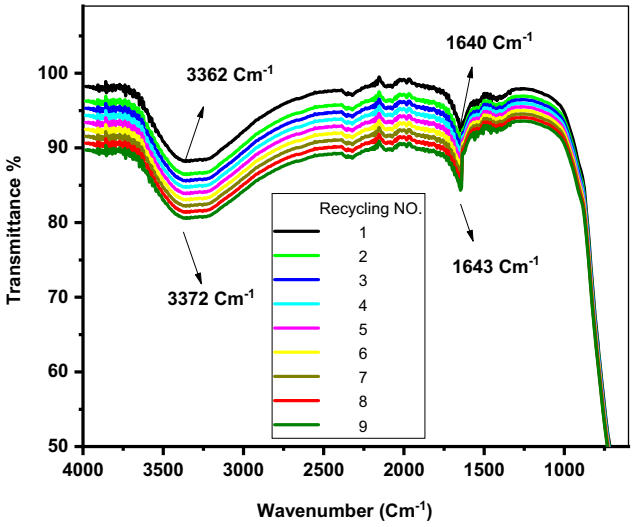

Figure 11: FTIR spectrum of TDS1 before and after recycling processes.

This result refers to an increase in the size of the TDS samples that is being studied; after nine cycles of recycling, no additional peaks are seen, which indicates that there has been no adsorption that has taken place on the catalyst surface, and variations in the frequency and relative band strengths of absorption bands suggest that there have been few modifications to the chemical structure.

Table 3: Antimicrobial activity of TDS1, TDS2, and TDS3 against different microorganisms

Microorganism		Inhibition zone (mm)		
		TDS1	TDS2	TDS3
Gram-positive bacterium	*B. subtilis*	18	14	10
Gram-negative bacterium	*S. enterica*	0	0	0
Yeast	*C. albicans*	10	12	15
Fungus	*A. niger*	0	0	0

3.9 *In vitro* antimicrobial activity

All TDS samples have antimicrobial activity against the gram-positive bacterium, *Bacillus subtilis*, and the yeast, *C. albicans*, as shown in Table 3 and Figure 12, while all TDS samples did not show any antimicrobial activity against the gram-negative (*S. enterica*) bacterium or antifungal activity (*Aspergillus niger*). The microbial gram-positive bacteria and yeast tests revealed that the inhibition zone for TDS1 was larger than that observed for TDS2 and TDS3 due to the enhanced antimicrobial activity of TDS1 referring to the high surface area for the TDS1 sample than other samples (TDS2 and TDS3) which have more reactive oxygen species as a generated free radical which led to increasing the inhibition zone.

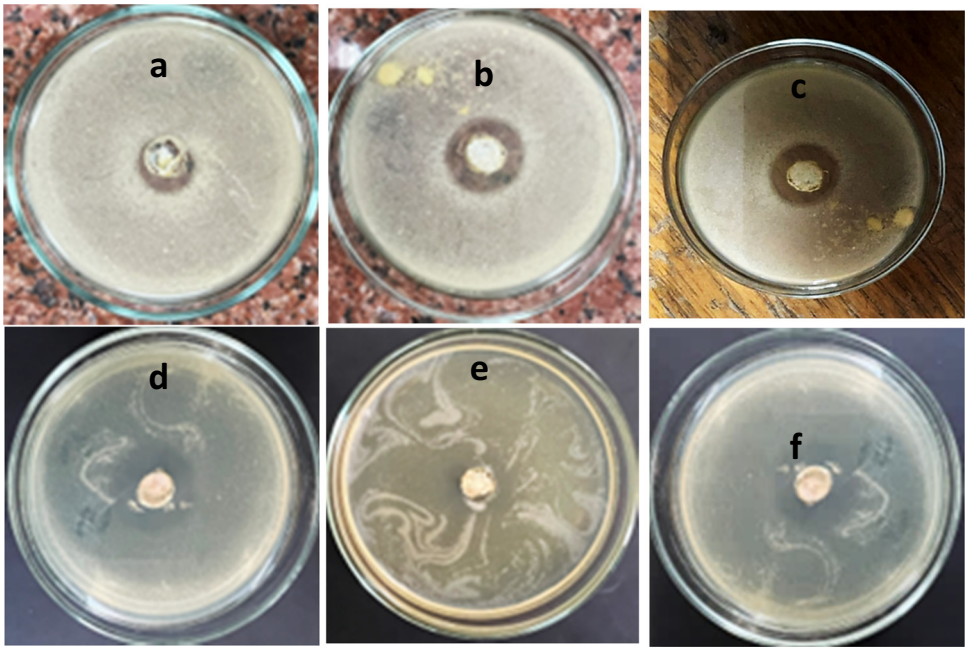

Figure 12: Inhibition zone of TDS1, TDS2, and TDS3 against *B. subtilis* (a)–(c) and *C. albicans* (d)–(f), respectively.

4 Conclusion

This study successfully synthesized TDS of sizes 3.1, 5.5, and 8.5 nm using a low-temperature precipitation technique followed by calcination at 280, 290, and 300°C, respectively. Extensive characterization using XRD, XPS, TEM, and FTIR verified the high crystallinity, anatase phase purity, and nano-scaled dimensions of the produced TDS particles. XRD analysis indicated an increase in crystallite size from 3.1 to 8.5 nm with increasing calcination temperature. XPS confirmed the chemical states of Ti, O, and C in TDS1. TEM imaging revealed spherical, elongated nanoparticles with sizes consistent with XRD data, along with high crystallinity. FTIR identified characteristic Ti–O–Ti vibrations in TDS.

Optical characterization showed the bandgap energy decreased from 3.09 to 2.97 eV for TDS1 to TDS3, respectively, due to the quantum confinement effect of the smaller 3.1 nm particles. Correspondingly, TDS1 exhibited a large surface area of 357.14 m^2/g. Photocatalytic testing demonstrated that TDS1 had the highest rate constant of 22.49×10^{-3} S^{-1} for degrading Congo red dye under the xenon lamp, compared to 14.30×10^{-3} and 9.81×10^{-3} S^{-1} for TDS2 and TDS3. The superior photocatalytic performance of TDS1 is ascribed to the increased bandgap and surface area from quantum confinement in the smaller 3.1 nm particles. TDS1 also showed excellent recyclability for degrading real industrial textile wastewater under sunlight over nine cycles. COD, TOC, and FTIR analysis verified stable photocatalytic performance upon reuse without changes in the chemical structure or species adsorption.

Additionally, all TDS samples displayed antimicrobial activity against *B. subtilis* and *C. albicans*, with TDS1 exhibiting the largest inhibition zone. This enhanced antimicrobial effect is due to the high surface area and increased reactive oxygen species generation of the 3.1 nm TDS1 particles. In summary, this work successfully synthesized pure anatase phase TDS with tunable properties by controlling calcination temperature. The optimal 3.1 nm TDS1 particles achieved superior photocatalytic performance for dye degradation and wastewater treatment due to the combined effects of increased bandgap and surface area from quantum size confinement.

Acknowledgments: The authors extend their appreciation to the Deanship of Scientific Research at King Khalid University for funding.

Funding information: The authors extend their appreciation to the Deanship of Scientific Research at King Khalid University for funding this work through a large group Research Project under grant number RGP2/258/44.

Author contributions: Walied A. A. Mohamed: conceptualization, data curation, writing – original draft. Hala H. Abd El-Gawad: formal analysis, data curation, writing – original draft. Hanan A. Mousa: formal analysis, data curation, writing – original draft. Hala T. Handal: formal analysis, data curation, writing – original draft. Hoda R. Galal: formal analysis, data curation. Ibrahem A. Ibrahem: writing – original draft. Ahmed Atef El-Beih: formal analysis, data curation. Mona M. Fawzy: formal analysis, data curation. Mahmoud A.M. Ahmed: formal analysis, data curation. Saleh D. Mekkey: formal analysis, data curation. Ammar A. Labib: conceptualization, data curation, writing – original draft. All authors have accepted responsibility for the entire content of this manuscript and approved its submission.

Conflict of interest: The authors state no conflict of interest.

References

[1] Udayakumar S, Praveen K. Chapter 16 - Advancements in industrial wastewater treatment by integrated membrane technologies. In: Kumar V, Kumar M, editors. Integrated environmental technologies for wastewater treatment and sustainable development. Amsterdam, Netherlands: Elsevier; 2022. p. 369–82.

[2] Singh P, Rani N, Kumar S, Kumar P, Mohan B, Pallavi, et al. Assessing the biomass-based carbon dots and their composites for photocatalytic treatment of wastewater. J Clean Prod. 2023;413:137474. doi: 10.1016/j.jclepro.2023.137474.

[3] Kong Z, Li L, Xue Y, Yang M, Li Y-Y. Challenges and prospects for the anaerobic treatment of chemical-industrial organic wastewater: A review. J Clean Prod. 2019;231:913–27. doi: 10.1016/j.jclepro.2019.05.233.

[4] Omran BA, Baek K-H. Valorization of agro-industrial biowaste to green nanomaterials for wastewater treatment: Approaching green chemistry and circular economy principles. J Environ Manag. 2022;311:114806. doi: 10.1016/j.jenvman.2022.114806.

[5] Agarkoti C, Thanekar PD, Gogate PR. Cavitation based treatment of industrial wastewater: A critical review focusing on mechanisms, design aspects, operating conditions and application to real effluents. J Environ Manag. 2021;300:113786. doi: 10.1016/j.jenvman.2021.113786.

[6] Lutz H, Weitzel HP, Huster W. 10.27 - Aqueous emulsion polymers. In: Matyjaszewski K, Möller M, editors. Polymer science: A comprehensive reference. Amsterdam: Elsevier; 2012. p. 479–518.

[7] Dhanjai, Sinha A, Zhao H, Chen J, Mugo SM. Water analysis | Determination of chemical oxygen demand. In: Worsfold P, Poole C, Townshend A, Miró M, editors. Encyclopedia of analytical science. 3rd edn. Oxford: Academic Press; 2019. p. 258–70.

[8] Al-Nuaim MA, Alwasiti AA, Shnain ZY. The photocatalytic process in the treatment of polluted water. Chem Pap. 2023;77:677–701. doi: 10.1007/s11696-022-02468-7.

[9] Kumar R, Raizada P, Khan AAP, Nguyen V-H, Van Le Q, Ghotekar S, et al. Recent progress in emerging $BiPO_4$-based photocatalysts: Synthesis, properties, modification strategies, and photocatalytic

applications. J Mater Sci Technol. 2022;108:208–25. doi: 10.1016/j.jmst.2021.08.053.
[10] Tanveer R, Yasar A, Nizami A-S, Tabinda AB. Integration of physical and advanced oxidation processes for treatment and reuse of textile dye-bath effluents with minimum area footprint. J Clean Prod. 2023;383:135366. doi: 10.1016/j.jclepro.2022.135366.
[11] Maheshwari U, Thakur RV, Deshpande D, Ghodke S. Efficiency evaluation of orange and banana peels for dye removal from synthetic industrial effluent. Mater Today: Proc. 2023;76:170–6. doi: 10.1016/j.matpr.2022.11.023.
[12] Ewuzie U, Saliu OD, Dulta K, Ogunniyi S, Bajeh AO, Iwuozor KO, et al. A review on treatment technologies for printing and dyeing wastewater (PDW). J Water Process Eng. 2022;50:103273. doi: 10.1016/j.jwpe.2022.103273.
[13] Singha K, Pandit P, Maity S, Sharma SR. Chapter 11 - Harmful environmental effects for textile chemical dyeing practice. In: Ibrahim N, Hussain CM, (Eds.). Green chemistry for sustainable textiles. Cambridge, UK: Woodhead Publishing; 2021. p. 153–64.
[14] Song X-L, Chen L, Gao L-J, Ren J-T, Yuan Z-Y. Engineering g-C_3N_4 based materials for advanced photocatalysis: Recent advances. Green Energy Environ. 2024;9:166–97. doi: 10.1016/j.gee.2022.12.005.
[15] Jabir MS, Mohammed MKA, Albukhaty S, Ahmed DS, Syed A, Elgorban AM, et al. Functionalized SWCNTs@Ag–TiO_2 nanocomposites induce ROS-mediated apoptosis and autophagy in liver cancer cells. 2023;12:20230127. doi: 10.1515/ntrev-2023-0127.
[16] Dutta V, Verma R, Gopalkrishnan C, Yuan M-H, Batoo KM, Jayavel R, et al. Bio-inspired synthesis of carbon-based nanomaterials and their potential environmental applications: A state-of-the-art review. Inorganics; 2022;10:169.
[17] Limón-Rocha I, Marizcal-Barba A, Guzmán-González CA, Anaya-Esparza LM, Ghotekar S, González-Vargas OA, et al. Co, Cu, Fe, and Ni deposited over TiO_2 and their photocatalytic activity in the degradation of 2,4-dichlorophenol and 2,4-dichlorophenoxyacetic Acid. Inorganics. 2022;10:157.
[18] Millbern Z, Trettin A, Wu R, Demmler M, Vinueza NR. Synthetic dyes: A mass spectrometry approach and applications. Mass Spectrom Rev. 2024;43:327–44. doi: 10.1002/mas.21818.
[19] Jędrzejewska B, Kabatc J, Pietrzak M, Pączkowski J. Hemicyanine dyes: Synthesis, structure and photophysical properties. Dye Pigment. 2003;58:47–58. doi: 10.1016/s0143-7208(03)00035-4.
[20] Sardar M, Manna M, Maharana M, Sen S. Remediation of dyes from industrial wastewater using low-cost adsorbents. In Environmental chemistry for a sustainable world. Cham, Switzerland: Springer International Publishing; 2020. p. 377–403
[21] Bao R, Zhang S, Li Y, Yang R, Xia J, Li H. Synthesize of in-situ polymerized PVDF/Fe-MILs membranes for highly efficient organic pollutants degradation and photocatalytic self-cleaning. J Phys Chem Solids. 2023;180:111463. doi: 10.1016/j.jpcs.2023.111463.
[22] Shabna S, Dhas SSJ, Biju CS. Potential progress in SnO2 nanostructures for enhancing photocatalytic degradation of organic pollutants. Catal Commun. 2023;177:106642. doi: 10.1016/j.catcom.2023.106642.
[23] Yadav M, Garg S, Chandra A, Hernadi K. Immobilization of green BiOX (X = Cl, Br and I) photocatalysts on ceramic fibers for enhanced photocatalytic degradation of recalcitrant organic pollutants and efficient regeneration process. Ceram Int. 2019;45:17715–22. doi: 10.1016/j.ceramint.2019.05.340.
[24] Ayodele BV, Alsaffar MA, Mustapa SI, Cheng CK, Witoon T. Modeling the effect of process parameters on the photocatalytic degradation of organic pollutants using artificial neural networks. Process Saf Environ Prot. 2021;145:120–32. doi: 10.1016/j.psep.2020.07.053.
[25] Sawunyama L, Oyewo OA, Seheri N, Onjefu SA, Onwudiwe DC. Metal oxide functionalized ceramic membranes for the removal of pharmaceuticals in wastewater. Surf Interfaces. 2023;38:102787. doi: 10.1016/j.surfin.2023.102787.
[26] Pattnaik A, Sahu JN, Poonia AK, Ghosh P. Current perspective of nano-engineered metal oxide based photocatalysts in advanced oxidation processes for degradation of organic pollutants in wastewater. Chem Eng Res Des. 2023;190:667–86. doi: 10.1016/j.cherd.2023.01.014.
[27] Wang Y, Selvakumar K, Oh TH, Arunpandian M, Swaminathan M. Boosting photocatalytic activity of single metal atom oxide anchored on TiO_2 nanoparticles: An efficient catalyst for photodegradation of pharmaceutical pollutants. J Alloy Compd. 2023;950:169821. doi: 10.1016/j.jallcom.2023.169821.
[28] Mohamed WAA, Abd El-Gawad HH, Handal HT, Galal HR, Mousa HA, ElSayed BA, et al. Study of phytotoxicity, remarkable photocatalytic activity, recycling process and energy consumption cost of TiO_2 quantum dots photocatalyst for photodegradation of Coomassie brilliant blue R dye. Opt Mater. 2023;137:113607. doi: 10.1016/j.optmat.2023.113607.
[29] Van Thuan D, Ngo HL, Thi HP, Chu TTH. Photodegradation of hazardous organic pollutants using titanium oxides -based photocatalytic: A review. Environ Res. 2023;229:116000. doi: 10.1016/j.envres.2023.116000.
[30] Zeshan M, Bhatti IA, Mohsin M, Iqbal M, Amjed N, Nisar J, et al. Remediation of pesticides using TiO_2 based photocatalytic strategies: A review. Chemosphere. 2022;300:134525. doi: 10.1016/j.chemosphere.2022.134525.
[31] Otitoju TA, Bai Y, Tian Y, Feng Z, Wang Y, Zhang X, et al. Surface modification of PVDF membrane *via* layer-by-layer self-assembly of TiO_2/V for enhanced photodegradation of emerging organic pollutants and the implication for wastewater remediation. Chem Eng Sci. 2023;275:118762. doi: 10.1016/j.ces.2023.118762.
[32] Velempini T, Prabakaran E, Pillay K. Recent developments in the use of metal oxides for photocatalytic degradation of pharmaceutical pollutants in water—a review. Mater Today Chem. 2021;19:100380. doi: 10.1016/j.mtchem.2020.100380.
[33] Gupta SK, Sudarshan K, Kadam RM. Optical nanomaterials with focus on rare earth doped oxide: A Review. Mater Today Commun. 2021;27:102277. doi: 10.1016/j.mtcomm.2021.102277.
[34] Tong S, Zhou J, Ding L, Zhou C, Liu Y, Li S, et al. Preparation of carbon quantum dots/TiO_2 composite and application for enhanced photodegradation of rhodamine B. Colloids Surf A: Physicochem Eng Asp. 2022;648:129342. doi: 10.1016/j.colsurfa.2022.129342.
[35] Moniruzzaman M, Deb Dutta S, Lim K-T, Kim J. Wet chemistry-based processing of tunable polychromatic carbon quantum dots for multicolor bioimaging and enhanced NIR-triggered photothermal bactericidal efficacy. Appl Surf Sci. 2022;597:153630. doi: 10.1016/j.apsusc.2022.153630.
[36] Vinayagam R, Pai S, Murugesan G, Varadavenkatesan T, Selvaraj R. Synthesis of photocatalytic zinc oxide nanoflowers using Peltophorum pterocarpum pod extract and their characterization. Appl Nanosci. 2023;13:847–57. doi: 10.1007/s13204-021-01919-z.

[37] Vinayagam R, Pai S, Varadavenkatesan T, Pugazhendhi A, Selvaraj R. Characterization and photocatalytic activity of ZnO nanoflowers synthesized using Bridelia retusa leaf extract. Appl Nanosci. 2023;13:493–502. doi: 10.1007/s13204-021-01816-5.
[38] Vinayagam R, Hebbar A, Senthil Kumar P, Rangasamy G, Varadavenkatesan T, Murugesan G, et al. Green synthesized cobalt oxide nanoparticles with photocatalytic activity towards dye removal. Environ Res. 2023;216:114766. doi: 10.1016/j.envres.2022.114766.
[39] Riad KB, Hoa SV, Wood-Adams PM. Metal oxide quantum dots embedded in silica matrices made by flame spray pyrolysis. ACS Omega. 2021;6:11411–17. doi: 10.1021/acsomega.0c06227.
[40] Mohamed WAA, El-Gawad HHA, Mekkey SD, Galal HR, Labib AA. Facile synthesis of quantum dots metal oxide for photocatalytic degradation of organic hazardous materials and factory effluents. Arab J Chem. 2022;15:103593. doi: 10.1016/j.arabjc.2021.103593.
[41] Chavali MS, Nikolova MP. Metal oxide nanoparticles and their applications in nanotechnology. SN Appl Sci. 2019;1:607. doi: 10.1007/s42452-019-0592-3.
[42] Wu H, Zhang D, Lei B-X, Liu Z-Q. Metal oxide based photoelectrodes in photoelectrocatalysis: Advances and challenges. ChemPlusChem. 2022;87:e202200097. doi: 10.1002/cplu.202200097.
[43] Alhalili Z. Metal oxides nanoparticles: General structural description, chemical, physical, and biological synthesis methods, role in pesticides and heavy metal removal through wastewater treatment. Molecules. 2023;28(7):3086. doi: 10.3390/molecules28073086.
[44] Tvrdy K, Frantsuzov PA, Kamat PV. Photoinduced electron transfer from semiconductor quantum dots to metal oxide nanoparticles. Proc Natl Acad Sci. 2011;108:29–34. doi: 10.1073/pnas.1011972107.
[45] Sadeghi SM, Wing WJ, Gutha RR. Perspective on functional metal-oxide plasmonic metastructures. J Appl Phys. 2023;133:070901. doi: 10.1063/5.0134141.
[46] Yadav S, Maurya PK. Biomedical applications of metal oxide nanoparticles in aging and age-associated diseases. 3 Biotech. 2021;11:338. doi: 10.1007/s13205-021-02892-8.
[47] Subhan MA. Advances with metal oxide-based nanoparticles as MDR metastatic breast cancer therapeutics and diagnostics. RSC Adv. 2022;12:32956–78. doi: 10.1039/d2ra02005j.
[48] Kotrange H, Najda A, Bains A, Gruszecki R, Chawla P, Tosif MM. Metal and metal oxide nanoparticle as a novel antibiotic carrier for the direct delivery of antibiotics. Int J Mol Sci. 2021;22(17):9596. doi: 10.3390/ijms22179596.
[49] Ribeiro AI, Dias AM, Zille A. Synergistic effects between metal nanoparticles and commercial antimicrobial agents: A review. ACS Appl Nano Mater. 2022;5:3030–64. doi: 10.1021/acsanm.1c03891.
[50] Fouda A, Alshallash KS, Alghonaim MI, Eid AM, Alemam AM, Awad MA, et al. The antimicrobial and mosquitocidal activity of green magnesium oxide nanoparticles synthesized by an aqueous peel extract of Punica granatum. Chemistry; 2023. p. 2009–24.
[51] Hassan SE, Fouda A, Saied E, Farag MMS, Eid AM, Barghoth MG, et al. Rhizopus oryzae-mediated green synthesis of magnesium oxide nanoparticles (MgO-NPs): A promising tool for antimicrobial, mosquitocidal action, and tanning effluent treatment. Journal of Fungi. 2021;7(5):372.
[52] Cruz-Luna AR, Cruz-Martínez H, Vásquez-López A, Medina DI. Metal nanoparticles as novel antifungal agents for sustainable agriculture: Current advances and future directions. J Fungi. 2021;7(12):1033. doi: 10.3390/jof7121033.
[53] Slavin YN, Bach H. Mechanisms of antifungal properties of metal nanoparticles. Nanomaterials (Basel). 2022;12. doi: 10.3390/nano12244470.
[54] Pan SRDT, Goudoulas TB, Jeevanandam J, Tan KX, Chowdhury S, Danquah MK. Therapeutic applications of metal and metal-oxide nanoparticles: Dermato-cosmetic perspectives. Front Bioeng Biotechnol. 2021;9:724499. doi: 10.3389/fbioe.2021.724499.
[55] Sachdeva V, Monga A, Vashisht R, Singh D, Singh A, Bedi N. Iron oxide nanoparticles: The precise strategy for targeted delivery of genes, oligonucleotides and peptides in cancer therapy. J Drug Delivery Sci Technol. 2022;74:103585. doi: 10.1016/j.jddst.2022.103585.
[56] Yoon Y, Truong PL, Lee D, Ko SH. Metal-oxide nanomaterials synthesis and applications in flexible and wearable sensors. ACS Nanosci Au. 2022;2:64–92. doi: 10.1021/acsnanoscienceau.1c00029.
[57] Al-Bataineh QM, Ahmad AA, Alsaad AM, Telfah AD. Optical characterizations of PMMA/metal oxide nanoparticles thin films: bandgap engineering using a novel derived model. Heliyon. 2021;7:e05952. doi: 10.1016/j.heliyon.2021.e05952.
[58] Shahid M, Sagadevan S, Ahmed W, Zhan Y, Opaprakasit P. 1 - Metal oxides for optoelectronic and photonic applications: A general introduction. In: Sagadevan S, Podder J, Mohammad F, editors. Metal oxides for optoelectronics and optics-based medical applications. Amsterdam, Netherlands: Elsevier; 2022. p. 3–31.
[59] Duque JS, Madrigal BM, Riascos H, Avila YP. Colloidal metal oxide nanoparticles prepared by laser ablation technique and their antibacterial test. Colloids and Interfaces. 2019;3(1):25.
[60] Sharif A, Farid N, O'Connor GM. Ultrashort laser sintering of metal nanoparticles: A review. Results Eng. 2022;16:100731. doi: 10.1016/j.rineng.2022.100731.
[61] Ungureanu C, Tihan GT, Zgârian RG, Fierascu I, Baroi AM, Răileanu S, et al. Metallic and metal oxides nanoparticles for sensing food pathogens-An overview of recent findings and future prospects. Materials (Basel). 2022;15(15):5374. doi: 10.3390/ma15155374.
[62] Maciulis V, Ramanaviciene A, Plikusiene I. Recent advances in synthesis and application of metal oxide nanostructures in chemical sensors and biosensors. Nanomaterials. 2022;12(24):4413.
[63] Liu X, Tao X, Xu C, Li X, Chen R, Chen Y, et al. Evaluation of the photocatalytic performance of molecularly imprinted S–TiO_2 by paper microzones. Environ Res. 2021;199:111258. doi: 10.1016/j.envres.2021.111258.
[64] El-Sayed BA, Mohamed WAA, Galal HR, Abd El-Bary HM, Ahmed MAM. Photocatalytic study of some synthesized MWCNTs/TiO_2 nanocomposites used in the treatment of industrial hazard materials. Egypt J Pet. 2019;28:247–52. doi: 10.1016/j.ejpe.2019.05.002.
[65] Mohamed WAA, Abd El-Gawad HH, Handal HT, Galal HR, Mousa HA, Elsayed BA, et al. TiO_2 quantum dots: Energy consumption cost,-germination, and phytotoxicity studies, recycling photo and solar catalytic processes of reactive yellow 145 dye and natural industrial wastewater. Adv Powder Technol. 2023;34:103923. doi: 10.1016/j.apt.2022.103923.
[66] Magaldi S, Mata-Essayag S, Hartung de Capriles C, Perez C, Colella MT, Olaizola C, et al. Well diffusion for antifungal susceptibility testing. Int J Infect Dis. 2004;8:39–45. doi: 10.1016/j.ijid.2003.03.002.
[67] Elmouwahidi A, Bailón E, Castelo-Quibén J, Perez-Cadenas A, Maldonado-Hódar FJ, Carrasco-Marín F. Carbon-TiO_2 composites as high-performance supercapacitor electrodes: Synergistic effect

between carbon and metal oxide phases. J Mater Chem A. 2017;6. doi: 10.1039/C7TA08023A.

[68] Leichtweiss T, Henning R, Koettgen J, Schmidt R, Holländer B, Martin M, et al. Amorphous and highly nonstoichiometric titania (TiO_x) thin films close to metal-like conductivity. J Mater Chem A: Mater Energy Sustainability. 2014;2:6631–40. doi: 10.1039/C3TA14816E.

[69] Mohamed WAA, El-Gawad HA, Mekkey S, Galal H, Handal H, Mousa H, et al. Quantum dots synthetization and future prospect applications. Nanotechnol Rev. 2021;10:1926–40. doi: 10.1515/ntrev-2021-0118.

[70] Mohamed WAA, Abd El-Gawad HH, Mousa HA, Handal HT, Galal HR, Ibrahem IA, et al. Photophysical properties, antimicrobial activity, energy consumption and financial cost of recycling of TiO_2 quantum dots *via* photomineralization processes of Vat Green dye and industrial dyeing effluents. Ceram Int. 2024;10(1):1926–40. doi: 10.1016/j.ceramint.2024.02.009.

[71] Ghobashy MM, Alkhursani SA, Alqahtani HA, El-damhougy TK, Madani M. Gold nanoparticles in microelectronics advancements and biomedical applications. Mater Sci Eng: B. 2024;301:117191. doi: 10.1016/j.mseb.2024.117191.

[72] Jing HH, Shati AA, Alfaifi MY, Elbehairi SEI, Sasidharan S. The future of plant based green carbon dots as cancer Nanomedicine: From current progress to future Perspectives and beyond. J Adv Res. 2024. doi: 10.1016/j.jare.2024.01.034.

[73] Subaer S, Fansuri H, Haris A, Misdayanti M, Irfanita R, Ramadhan I, et al. Pervaporation membranes for seawater desalination based on Geo–rGO–TiO_2 nanocomposites. Part 1: Microstructure properties. Membranes. 2021;11:966. doi: 10.3390/membranes11120966.

[74] Hsu C-Y, Mahmoud ZH, Abdullaev S, Ali FK, Ali Naeem Y, Mzahim Mizher R, et al. Nano titanium oxide (nano-TiO_2): A review of synthesis methods, properties, and applications. Case Stud Chem Environ Eng. 2024;9:100626. doi: 10.1016/j.cscee.2024.100626.

[75] Ryu S, Jung YM. Positional fluctuation of IR absorption peaks: Frequency shift of a single band or relative intensity changes of overlapped bands? Am Lab. 2011;43:40–3.

[76] Srivastava A, Dangi LK, Kumar S, Rani R. Microbial decolorization of Reactive Black 5 dye by Bacillus albus DD1 isolated from textile water effluent: Kinetic, thermodynamics & decolorization mechanism. Heliyon. 2022;8:e08834. doi: 10.1016/j.heliyon.2022.e08834.

[77] Moyo S, Makhanya BP, Zwane PE. Use of bacterial isolates in the treatment of textile dye wastewater: A review. Heliyon. 2022;8:e09632. doi: 10.1016/j.heliyon.2022.e09632.

[78] Khaled JM, Alyahya SA, Govindan R, Chelliah CK, Maruthupandy M, Alharbi NS, et al. Laccase producing bacteria influenced the high decolorization of textile azo dyes with advanced study. Environ Res. 2022;207:112211. doi: 10.1016/j.envres.2021.112211.

[79] Bharatbhai Vishani D, Shrivastav A. Chapter 19 - Enzymatic decolorization and degradation of azo dyes. In: Shah MP, Rodriguez-Couto S, Kapoor RT, editors. Development in Wastewater Treatment Research and Processes. Elsevier; 2022. p. 419–32.

[80] Law KE. KSA Environment Law. In: https://leap.unep.org/countries/sa/national-legislation/royal-decree-nom165-2020-issuing-environment-law (Ed.) Royal Decree No.M/165 of 2020 issuing the Environment Law, UN Environmental Programme; 2020. https://leap.unep.org/countries/sa/national-legislation/royal-decree-nom165-2020-issuing-environment-law.

[81] Aziz G, Sarwar S. Revisit the role of governance indicators to achieve sustainable economic growth of Saudi Arabia – pre and post implementation of 2030 Vision. Struct Change Econ Dyn. 2023;66:213–27. doi: 10.1016/j.strueco.2023.04.008.